

This discussion paper is/has been under review for the journal Ocean Science (OS).
Please refer to the corresponding final paper in OS if available.

X-band COSMO-SkyMed[®] SAR data for sea wave simulations and coastal vulnerability assessment

G. Benassai¹, A. Montuori², M. Migliaccio², and F. Nunziata²

¹Dipartimento di Scienze Applicate, Università di Napoli Parthenope, Napoli, Italy

²Dipartimento di Tecnologie, Università di Napoli Parthenope, Napoli, Italy

Received: 19 September 2012 – Accepted: 2 October 2012 – Published: 17 October 2012

Correspondence to: A. Montuori (antonio.montuori@uniparthenope.it)

Published by Copernicus Publications on behalf of the European Geosciences Union.

OSD

9, 3281–3330, 2012

COSMO-SkyMed[®] for
coastal marine
applications

G. Benassai et al.

Title Page

Abstract

Introduction

Conclusions

References

Tables

Figures

◀

▶

◀

▶

Back

Close

Full Screen / Esc

Printer-friendly Version

Interactive Discussion



Abstract

In this paper, X-band COSMO-SkyMed[®] Synthetic Aperture Radar (SAR) data are first experimented as wind field forcing of coastal wind-wave oceanographic modeling for both sea-wave numerical simulation and coastal vulnerability assessment purposes. The SAR data set consists of 60 X-band VV-polarized Level 1B Detected Ground Multi-look (DGM) ScanSAR Huge Region COSMO-SkyMed[®] SAR measurements, collected in the test area of the Southern Tyrrhenian Coastal basin during the winter season of 2010. On one hand, the wind-wave oceanographic modeling is based on the third-generation Simulating WAVes Nearshore (SWAN) model, which is used for sea wave state estimation in coastal and island regions. On the other hand, the coastal vulnerability assessment model is based on the use of a key parameter known as impact index, which consistently provides the coastal risk evaluation due to the inundation of the in-shore land. Experiments consist of numerical wave simulations of the SWAN model accomplished with respect to some relevant wave storms recorded in the test area during the winter season of 2010. The wind forcing is provided by X-band COSMO-SkyMed[®] SAR-based wind field estimations which are properly blended with both buoys wave data and ECMWF model winds to retrieve meaningful wave parameters (e.g. significant wave height, wave directions and periods) as physical descriptors of tidal events. The output of numerical wave simulations are used to perform the coastal vulnerability assessment in the considered test area along the coastal plain of river Sele. The assessment is accomplished in terms of wave run-up height, storm beach retreat and both short- and long-term erosion shoreline evolution. Experimental results accomplished with X-band COSMO-SkyMed[®] SAR-based wind field forcing are successfully compared with the ones gathered by using both buoys wave field data and ECMWF model winds, only. They demonstrate that both wind-wave interaction modeling and coastal vulnerability assessment can take full benefits of blended wind field products composed by X-band COSMO-SkyMed[®] SAR wind field estimations and model data.

COSMO-SkyMed[®] for coastal marine applications

G. Benassai et al.

Title Page

Abstract

Introduction

Conclusions

References

Tables

Figures



Back

Close

Full Screen / Esc

Printer-friendly Version

Interactive Discussion



1 Introduction

The physical, chemical and biological interactions between the ocean and the atmosphere are of great applicative relevance to understand, characterize and predict their influence on both climate variability and Earth system dynamics (Janssen, 2004; Harlan, 2005). The key role of both the oceans and atmosphere in the planet's climate change results from their large capability to store and exchange energy in the form of heat, moisture, and momentum (Janssen, 2004; Harlan, 2005). Changes in the energy balance between the oceans and atmosphere account for a lot of coupled ocean-air circulation dynamics, which severely affect the global warming and the climate engine of the planet on a large space-temporal scale (Janssen, 2004; Harlan, 2005). In fact, the frictional drag of the wind on the ocean surface layer creates wave currents that can transport and redistribute fresh water, heat, salt and carbon dioxide to different ocean layers. Furthermore, the ocean waves transfer energy and momentum to the ocean through the process of white capping, thereby feeding the turbulent large-scale motions of the oceans (Janssen, 2004; Harlan, 2005). The monitoring and the forecasting of these wind-wave interaction processes become particularly critical along the coastal areas (Benassai, 2006; Di Paola, 2011; Alberico et al., 2012). These latter are highly dynamic and geomorphologic complex systems that respond in a non-linear manner to both extreme weather conditions and more generally external perturbations (Benassai, 2006; Di Paola, 2011; Alberico et al., 2012). In addition, the impact of climate change along the coastal regions may include the presence of meaningful events that severely affect the Earth system dynamics, such as the possible increase of sea surface temperatures, variability in the patterns of rainfall and runoff, changes in frequency, intensity and duration of wave storms (Benassai, 2006; Di Paola, 2011; Alberico et al., 2012).

Based on this rationale, the evolution of winds, waves and the wind-driven sea circulation is of great applicative relevance not only for the modeling and the forecasting of both weather and climate, but even for the observation of both oceanographic

OSD

9, 3281–3330, 2012

COSMO-SkyMed[®] for coastal marine applications

G. Benassai et al.

Title Page

Abstract

Introduction

Conclusions

References

Tables

Figures



Back

Close

Full Screen / Esc

Printer-friendly Version

Interactive Discussion



vulnerability by using a new parameter, known as impact index, which is based on wave, climate, bathymetry and sediment data. It depends on run-up height, seasonal and long-term erosion index, and efficiency of coastal protection structures (Benassai et al., 2009).

In this paper, both sea wave numerical simulations and the coastal vulnerability assessment are properly accomplished in a coastal environment by means of wind field forcing provided by X-band COSMO-SkyMed[®] SAR-based wind field retrievals. The SAR data set consists of 60 X-band VV-polarized Level 1B Detected Ground Multi-look (DGM) ScanSAR Huge Region mode COSMO-SkyMed[®] SAR measurements collected in the Southern Tyrrhenian Coastal area on 2010. Sea wave numerical simulations are accomplished through the SWAN model with respect to some relevant wave storms recorded in the considered test area during the winter season of 2010. A blended wind field product is provided as wind forcing of the SWAN model, which consists of X-band COSMO-SkyMed[®] SAR-based wind field (i.e. wind speed and direction) retrievals and either buoys wave field or ECMWF model data. Within such a framework, the SAR-based wind speed estimation is accomplished by means of the Azimuth cut-off procedure (Chapron et al., 1995; Kerbaol, 1998; Korsbakken et al., 1998; Migliaccio et al., 2012; Montuori et al., 2012), while the SAR-based wind direction retrieval is accomplished by using the Multi-Resolution Analysis of Discrete Wavelet Transform (MRA-DWT) (Du et al., 2002). The output of SWAN model numerical simulations allows providing relevant wave parameters (e.g. significant wave height, wave directions and periods), which are used not only as physical descriptors of tidal events, but also as the input of the coastal vulnerability assessment approach based on the use of the impact index described in (Benassai et al., 2009). The assessment is accomplished along the coastal plain of river Sele in terms of wave run-up height, storm beach retreat and both short- and long-term erosion shoreline evolution. The experimental results gathered with X-band COSMO-SkyMed[®] SAR-based wind field forcing are finally compared with the ones provided by using both buoys wave field data and ECMWF model winds, only. The comparison is accomplished to analyze the

COSMO-SkyMed[®] for coastal marine applications

G. Benassai et al.

Title Page

Abstract

Introduction

Conclusions

References

Tables

Figures



Back

Close

Full Screen / Esc

Printer-friendly Version

Interactive Discussion



capabilities of blended wind field products composed by X-band COSMO-SkyMed[®] SAR wind field estimations and model data both in terms of sea wave numerical simulations and coastal vulnerability assessment purposes.

The paper is organized as follows: the test area and the data set used in this study are fully detailed in Sect. 2. The theoretical background and the methodology at the basis of (1) X-band SAR-based wind field retrieval, (2) SWAN model and (3) coastal vulnerability assessment is briefly described in Sect. 3. Experimental results relevant to the X-band SAR-based wind field retrieval, sea wave numerical simulations and coastal risk evaluations are presented and discussed in Sect. 4. Conclusions are finally drawn in Sect. 5.

2 Data set

In this section, the test area and the data set used for both sea wave numerical simulations and coastal vulnerability assessments purposes are fully detailed.

The test area is the coastal zone of the Southern Tyrrhenian Sea, including the Gulfs of Gaeta, Napoli, Salerno and Policastro, which are of great applicative relevance for both oceanographic and coastal-maritime surveillance purposes.

The data set consists of:

- 60 X-band VV-polarized Level 1B DGM ScanSAR Huge Region COSMO-SkyMed[®] SAR data, gathered in the test area during the winter season of 2010 (Italian Space Agency, 2007). They provide ground coverage of about 200km × 200km with a spatial resolution of 100m × 100m. Each SAR data is characterized by large variability for the incidence angle θ ($\sim 10^\circ$) and the whole SAR data set allows covering a broad range of θ values (25° – 60°). Moreover, each Level 1B DGM SAR data accounts for a huge number of looks (~ 18) (Italian Space Agency, 2007).

OSD

9, 3281–3330, 2012

COSMO-SkyMed[®] for coastal marine applications

G. Benassai et al.

Title Page

Abstract

Introduction

Conclusions

References

Tables

Figures



Back

Close

Full Screen / Esc

Printer-friendly Version

Interactive Discussion



- Timely and spatially co-located European Centre for Medium Weather Forecast (ECMWF) model data (<http://www.ecmwf.int/>), with a spatial gridding resolution of 0.2° ($\sim 20\text{ km} \times 20\text{ km}$) and a time resolution of 6 h.
- Timely and spatially co-located wave field data provided by in situ National and Regional buoys system observations (http://www.idromare.it/analisi_dati.php). In particular, national wave data have been retrieved by Rete Ondametrica Nazionale (RON), on the locations of Ponza (on the Northern bound of the Gulf of Gaeta) and Cetraro (on the Southern bound of the Gulf of Policastro), while the regional wave data have been retrieved by the Campania buoy network on the locations of Capri (off-shore the Gulf of Naples) and offshore Acciaroli (in the Gulf of Salerno).

3 Methodology

In this section, the theoretical background and the methodology at the basis of the sea wave numerical simulations and coastal vulnerability assessment by means of X-band COSMO-SkyMed[®] SAR-based wind field estimations is briefly described.

3.1 X-band SAR wind field retrieval algorithm

The methodology and the physical background of the X-band SAR-based wind field retrieval approach is here presented and properly detailed for X-band VV-polarized Level 1B DGM ScanSAR Huge Region mode COSMO-SkyMed[®] SAR data.

Since the SAR-based wind field estimation is strongly affected by SAR data quality, a pre-processing analysis has been accomplished, which aims at improving the image quality of X-band VV-polarized Level 1B DGM ScanSAR Huge Region mode COSMO SkyMed[®] SAR measurements. In fact, on one side, X-band SAR data may be severely affected by tropospheric and atmospheric phenomena (e.g. rain cells, cloud coverage,

Title Page

Abstract

Introduction

Conclusions

References

Tables

Figures



Back

Close

Full Screen / Esc

Printer-friendly Version

Interactive Discussion



oceanic fronts, convective cells, etc.) that, especially at higher frequencies, can drastically hamper both the SAR imagery interpretability and therefore the retrieval of some meaningful geophysical parameters, such the sea surface wind field (Lee et al., 1995). On the other side, the peculiar burst acquisition mode of ScanSAR SAR measurements is characterized by the presence of the scalloping, i.e. periodic processing anomalies along with the azimuth direction that, appearing as bars in SAR imagery, strongly affects the accuracy of SAR-based wind field estimation (Schiavulli et al., 2011, 2012).

With this respect, an automatic two-steps pre-processing procedure, first developed in (Schiavulli et al., 2011), has been here adopted to effectively account for both the above-mentioned phenomena and therefore improve the quality of SAR images. The first step aims at removing the scalloping pattern in X-band ScanSAR COSMO-SkyMed[®] SAR data by means of a filtering technique based on the Discrete Wavelet Transform Multi Resolution Analysis (DWT-MRA) (Mallat, 1989; Schiavulli et al., 2011, 2012). The proposed approach naturally describes the directional features of an image at different spatial scales and therefore it is able to both highlight and then remove the scalloping pattern, which is related to the SAR image spectrum. As demonstrated in (Schiavulli et al., 2011, 2012) for the specific COSMO-SkyMed[®] SAR data product, it was not possible for the users to reprocess the SAR raw data and therefore only a sub-optimal de-scalloping post-processing procedure had to be taken into account. The second step of the pre-processing procedure allows detecting and then removing all the atmospheric phenomena in X-band SAR data by means of a homogeneity test based on the variance to mean square ratio (VMSR) of SAR image power spectral density (Schultz-Stellenfleth et al., 2004; Schiavulli et al., 2011). The proposed approach is able to univocally discriminate among sea, i.e. homogeneous, and non-homogeneous parts of SAR images, such as ships, coastline and atmospheric fronts.

Following the pre-processing analysis, the SAR-based wind field retrieval is accomplished by means of a two-step procedure, which allows estimating the sea surface wind speed and wind direction, independently.

**COSMO-SkyMed[®] for
coastal marine
applications**

G. Benassai et al.

Title Page

Abstract

Introduction

Conclusions

References

Tables

Figures



Back

Close

Full Screen / Esc

Printer-friendly Version

Interactive Discussion



The SAR-based wind speed estimation is accomplished by means of a SAR wind speed algorithm based on the Azimuth cut-off procedure (Chapron et al., 1995; Kerbaol, 1998; Korsbakken et al., 1998; Migliaccio et al., 2012; Montuori et al., 2012), which allows consistently retrieving the sea surface wind speed without requiring both any a priori wind direction information and the calibration accuracy of SAR normalized radar cross section (NRCS) measurements of the observed scene. The physical rationale at the basis of the proposed approach lies on the well-known azimuthal Doppler mis-registration due to the orbital motion of sea surface waves, which affects the sea surface SAR imaging, based on both sensor's parameters (e.g. platform altitude, velocity, etc.) and sea state conditions (Chapron et al., 1995; Kerbaol, 1998; Korsbakken et al., 1998). It limits the shortest detectable wavelength in the azimuth direction λ_c , which has been demonstrated to be a key cinematic parameter that, accounting for sea waves orbital motions within SAR integration time, can be considered a robust indicator of the sea surface wind speed (Chapron et al., 1995; Kerbaol, 1998; Korsbakken et al., 1998). Based on this rationale, a SAR wind speed algorithm based on the Azimuth cut-off procedure has been developed and tested for C-band SAR measurements only (Chapron et al., 1995; Kerbaol, 1998; Korsbakken et al., 1998), where λ_c is retrieved from the noise-free SAR auto-correlation function (ACF) and physically related to the sea surface wind speed according to the following linear semi-empirical model:

$$U_{10} = a(\lambda_c - \Lambda), \quad (1)$$

where U_{10} (m s^{-1}) is the wind speed at 10 m above the sea surface, Λ (m) is the SAR nominal azimuth resolution and a (1 s^{-1}) is an empirical parameter. Following this theoretical background, the physical rationale at the basis of the Azimuth cut-off procedure has been successfully extended and tested to the X-band VV-polarized Level 1B DGM ScanSAR Huge Region mode COSMO-SkyMed[®] SAR measurements (Migliaccio et al., 2012; Montuori et al., 2012).

COSMO-SkyMed[®] for coastal marine applications

G. Benassai et al.

Title Page

Abstract

Introduction

Conclusions

References

Tables

Figures



Back

Close

Full Screen / Esc

Printer-friendly Version

Interactive Discussion



spectrum N is considered rather than the energy density spectrum $E(\sigma, \theta)$, since in the presence of ambient currents only the action density is conserved (Whitham, 1974). The evolution of the wave spectrum is described by the spectral action balance equation (Hasselmann et al., 1973):

$$5 \quad \frac{\partial}{\partial t} N + \frac{\partial}{\partial x} c_x N + \frac{\partial}{\partial y} c_y N + \frac{\partial}{\partial \sigma} c_\sigma N + \frac{\partial}{\partial \theta} c_\theta N = \frac{S}{\sigma}, \quad (2)$$

where S is the effect of the difference between the inner and the outer energy for the spectrum F and σ is the intrinsic frequency. The first term on the left-hand side of Eq. (2) represents the timely-change rate of the local action density spectrum. The second and third term on the left-hand side of Eq. (2) represents the propagation of the action density spectrum in the Cartesian coordinates space, with propagation velocities c_x and c_y . The fourth term on the left-hand side of Eq. (2) represents the shifting of the relative frequency in the action density spectrum due to variations in depths and currents, with a propagation velocity c_σ . The fifth term on the left-hand side of Eq. (2) represents both the depth- and the current-induced refraction of the local action density spectrum, with propagation velocity c_θ . The term at the right-hand side of the action balance Eq. (2) is the source term of the energy density, representing the effects of generation, dissipation, and non-linear wave-wave interactions.

The SWAN model is operational at Dipartimento di Scienze Applicate (DSA) of the University of Naples Parthenope since January 2005 and is adopted for simulating both waves generation and propagation in the Gulf of Naples. The model is typically forced by using the wind field forcing at 1-h intervals provided through the Advanced Research Weather Research and Forecast (WRF-ARW) wind field model data, i.e. the next-generation mesoscale numerical weather model predictions that are designed to serve both operational forecasting and atmospheric research needs (Holthuisen et al., 1993; Booij et al., 1999; Benassai, 2006; Benassai et al., 2006). The model is implemented on nested grids, with an implicit numerical propagation scheme, which implies that the computations are more economic in shallow water (Holthuisen et al., 1993;

Title Page	
Abstract	Introduction
Conclusions	References
Tables	Figures
◀	▶
◀	▶
Back	Close
Full Screen / Esc	
Printer-friendly Version	
Interactive Discussion	



Booij et al., 1999; Benassai, 2006; Benassai et al., 2006). Outputs from the SWAN model include significant wave height (H_s) on gridded fields, with the associated wave directions (D_w) and periods (T_p), and the wave energy spectral information at different wavelengths.

3.3 Coastal vulnerability assessment

In this sub-section, the theoretical background and the methodology at the basis of the coastal vulnerability assessment is briefly outlined.

The approach proposed in this paper for the assessment of coastal vulnerability due to the inundation of the inshore land is based on the methodology developed and suggested in (Benassai et al., 2009), where a new key parameter known as impact index I_i is properly used for the coastal flooding risk evaluation. The new parameter accounts for wave climate, bathymetry and sediment data and depends on the wave run-up height, the seasonal and long-term erosion index, and the efficiency of coastal protection structures. It can be calculated according to the following model equation (Benassai et al., 2009):

$$I_i = I_{Ru} + I_R + I_D + E + T, \quad (3)$$

where I_{Ru} is a distance index associated to the wave run-up, I_R is the short-term erosion index for the shoreline, I_D is the index of stability for backshore coastal protection structures, E is the long-term erosion index and T is the tidal range.

Compared to the main methods developed for the coastal vulnerability assessment, this methodology can be applied on a small geographical scale for the definition of the coastal flooding risk evaluation. Moreover, it must be pointed out that the tidal effects are not considered in (Benassai et al., 2009) since the experimental application is relevant to the Mediterranean Sea, which is a micro-tidal coastal environment.

In this paper, the coastal vulnerability assessment is carried out by evaluating the impact index I_i without considering both the index of stability for backshore coastal protection structures I_D and the tidal range T . In fact, on one side, the coastal vulnerability

Title Page

Abstract

Introduction

Conclusions

References

Tables

Figures



Back

Close

Full Screen / Esc

Printer-friendly Version

Interactive Discussion



assessment is provided in the Southern Tyrrhenian Coastal basin, which is a micro-tidal ambient. On the other side, no coastal protection on the considered coastline stretch are taken into account in the work carried out in this paper. As a matter of fact, the evaluation of the impact index I_i is here accomplished by considering only the contribution of the wave run-up height (I_{Ru}), the short-term and the long-term erosion indexes (I_R and E).

The wave run-up height index (I_{Ru}) provides a measurement of the potential inundation capacity and is retrieved according to the empirical approach proposed in (Stockdon et al., 2006), where I_{Ru} is evaluated through the 2% exceedance level for run-up peaks (R) on natural beaches:

$$R_{2\%} = 1.1 \cdot \left(0.35 \cdot \beta_f \cdot (H_0 \cdot L_0)^{1/2} + \frac{[H_0 \cdot L_0 \cdot (0.563\beta_f^2 + 0.004)]^{1/2}}{2} \right). \quad (4)$$

β_f is the foreshore beach slope defined over the area of significant swash activity, while the wave length L_0 can be expressed in terms of the wave period by means of the linear dispersion relationship, $L_0 = gT^2/2\pi$. Equation (4) takes into account also the increase in water level due to wave set-up, which constitutes the main part of the increase in mean sea level, so the other terms of wind set-up and inverter barometer are properly neglected.

The short-term erosion index (I_R) provides a measurement of potential beach retreat and is used for the dynamical calculation of the shoreline retreat based on the convolution method of Kriebel and Dean (2003) that concerns the response of the equilibrium

Title Page

Abstract

Introduction

Conclusions

References

Tables

Figures

◀

▶

◀

▶

Back

Close

Full Screen / Esc

Printer-friendly Version

Interactive Discussion



beach profile during sea storms:

$$R(t) = \frac{R_{\infty}}{T_s} \int_0^t f(\tau) \exp[-(t-\tau)/T] \partial\tau \quad (5)$$

$$R_{\infty} = S \frac{W_b - d_b/m_0}{B + d_b - S/2}, \quad (6)$$

5 where:

S = Sea level increase due to wave storm;

B = berm height;

m_0 = slope of the seabed in the foreshore;

d_b = breaking depth;

10 W_b = offshore breaking depth distance.

The Kriebel and Dean convolution solution is given by:

$$\frac{R(t)}{R_{\infty}} = \frac{1}{2} \left\{ 1 - \frac{\beta^2}{1+\beta^2} \exp(-2\sigma t/\beta) - \frac{1}{1+\beta^2} [\cos(2\sigma t) + \beta \sin(2\sigma t)] \right\}, \quad (7)$$

where β is the ratio between the time scale of beach erosion T_s and the storm duration T_D :

$$15 \quad \beta = 2\pi T_s/T_D, \quad (8)$$

$$T_s = 320 \frac{H_b^{3/2}}{g^{1/2} A^3} \left(1 + \frac{d_b}{B} + \frac{m_0 W_b}{d_b} \right)^{-1}. \quad (9)$$

The maximum value of Eq. (7) is indicated as R_{\max}/R_{∞} and greatly depends on β and T_D .

The long-term erosion index (E) finally provides the long-term evaluation of potential beach retreat and is properly evaluated by comparing photogrammetric flights of different years relevant to the observed test area.

Experimental results relevant to the evaluation of run-up height, short-term and long-term potential beach erosion are both transformed in the corresponding vulnerability indexes and properly classified according to the scheme shown in Table 1. The classification of the run-up index I_{Ru} is based on the computation of the run-up width and is made non-dimensional with respect to the beach width. The classification of the short-term beach retreat index I_R is based on the computation of the short-term beach retreat width and again is made non-dimensional with respect the beach width. The classification of long-term index I_E is based on the computation of the long-term beach retreat.

Finally, the single scores relative to each index are properly combined in a global vulnerability index in order to classify each profile in terms of coastal vulnerability.

4 Experimental results

In this section, some meaningful experimental results are presented and discussed, which are relevant to both the application of the SWAN model in a coastal environment and the subsequent assessment of the coastal vulnerability, with forcing provided by COSMO-SkyMed[®] SAR-derived wind field estimations. Before proceeding to the description of the experimental results relevant to both the sea wave numerical simulations and the coastal vulnerability assessment, a preliminary analysis about the effectiveness of X-band COSMO-SkyMed[®] SAR-derived wind field estimation is provided, which aims at both validating the X-band SAR-based wind field product and therefore evaluating its consistency as wind field forcing for the wind-wave oceanographic modeling.

Title Page

Abstract

Introduction

Conclusions

References

Tables

Figures

⏪

⏩

◀

▶

Back

Close

Full Screen / Esc

Printer-friendly Version

Interactive Discussion



4.1 SAR wind field retrieval

In this sub-section some meaningful results are described, which are relevant to the X-band COSMO-SkyMed[®] SAR-derived wind field (i.e. wind speed and wind direction) estimation based on the wind field retrieval approach described in Sect. 3.1.

5 The ground truth, which is used as reference wind field for both comparison and validation purposes, is provided by timely and spatially co-located ASCAT scatterometer wind fields (<http://podaac.jpl.nasa.gov>), with a spatial gridding resolution of 12.5 km × 12.5 km. In the particular case where the ASCAT scatterometer ground truth is not available for the X-band COSMO-SkyMed[®] SAR acquisition, the reference ground truth is then provided by European Centre for Medium Weather Forecast (ECMWF) model data (<http://www.ecmwf.int/>), with a spatial resolution of 0.2° (20 km × 20 km).
10 Since the reference ground truth wind field (both the ASCAT scatterometer and the ECMWF model ones) is not always both timely co-located with respect to the SAR image acquisition, a linear interpolation in time is accomplished between the ground truth reference wind field data acquired before and after the SAR acquisition time, thus providing the timely co-located reference wind field. Moreover, since the reference ground truth is available at the given resolution gridding scale of both 12.5 km × 12.5 km and 20 km × 20 km for the ASCAT scatterometer and the ECMWF model wind field, respectively, a bi-linear spatially interpolation of the timely co-located wind field is accomplished inside of the spatial domain of SAR image at the specific SAR sub-image gridding scale ($N \times N$) used for wind field retrieval purposes.

A single experiment is fully detailed to demonstrate the consistency of the X-band COSMO-SkyMed[®] SAR-derived wind field retrieval, taking full benefits of VV-polarized Level 1B DGM ScanSAR Huge Region mode COSMO-SkyMed[®] SAR data.

25 The experiment is relevant to the X-band COSMO-SkyMed[®] SAR acquisition of 17 December 2010 at 18:00 UTC, which refers to an interesting wave storm occurred in the Tyrrhenian Sea coastal area during the winter season of 2010. The VV-polarized normalized radar cross-section (NRCS) image is shown in gray tones in Fig. 1a,

OSD

9, 3281–3330, 2012

COSMO-SkyMed[®] for coastal marine applications

G. Benassai et al.

Title Page

Abstract

Introduction

Conclusions

References

Tables

Figures

⏪

⏩

◀

▶

Back

Close

Full Screen / Esc

Printer-friendly Version

Interactive Discussion



where the scalloping effect and weak atmospheric phenomena are present. The output of the pre-processing step is shown in Fig. 1b, where the land masking is applied too. It must be noted that SAR image quality is successfully improved by sorting out both scalloping and atmospheric phenomena. The output of the X-band COSMO-SkyMed[®] SAR wind speed retrieval approach based on the Azimuth cut-off procedure is shown in Fig. 2a–c for the three reference SAR sub-image gridding scales used for wind speed estimation purposes, i.e. 12.5 km × 12.5 km, 6.25 km × 6.25 km and 3.125 km × 3.125 km, respectively. The reference ground truth is properly shown in Fig. 2d, e, which is provided by both timely and spatially co-located ECMWF model wind data and ASCAT scatterometer wind speed, respectively. It must be noted that in this particular case, the ASCAT scatterometer ground truth does not cover the whole spatial domain of the SAR acquisition (see Fig. 2f). The comparison between the X-band SAR-based Azimuth cut-off wind speed estimation and the reference ground truth (both the scatterometer- and the model-based wind speed) shows a fair agreement with root mean square error (RMSE) values lower than 3 ms⁻¹. In fact, the COSMO-SkyMed[®] SAR-ASCAT wind speed inter-comparison allows providing RMSE values, which are equal to 0.96 ms⁻¹, 1.5 ms⁻¹ and 1.7 ms⁻¹ for the three sub-image gridding scales of 12.5 km × 12.5 km, 6.25 km × 6.25 km and 3.125 km × 3.125 km, respectively. On the other side, the COSMO-SkyMed[®] SAR-ECMWF wind speed inter-comparison allows providing RMSE values, which are equal to 1.9 ms⁻¹, 1.4 ms⁻¹ and 1.6 ms⁻¹ for the three sub-image gridding scales of 12.5 km × 12.5 km, 6.25 km × 6.25 km and 3.125 km × 3.125 km, respectively. Experimental results demonstrate that the X-band COSMO-SkyMed[®] SAR wind speed estimations provided over the three different SAR sub-image gridding scales (i.e. 12.5 km × 12.5 km, 6.25 km × 6.25 km and 3.125 km × 3.125 km, respectively) are both consistent with respect to the provided reference ground truth and effectively comparable among them. This further demonstrates the effectiveness of the SAR-based wind speed retrieval approach, showing that the physical rationale of the X-band Azimuth cut-off model function does not profoundly change at the three different SAR sub-image gridding scales. However, it can be noted

**COSMO-SkyMed[®] for
coastal marine
applications**

G. Benassai et al.

Title Page

Abstract

Introduction

Conclusions

References

Tables

Figures



Back

Close

Full Screen / Esc

Printer-friendly Version

Interactive Discussion



that non-negligible differences in terms of sea surface wind speed are present along the coastal area of SAR image domain, for both ECMWF and ASCAT scatterometer winds. In fact, X-band SAR-derived wind speed retrievals are able to catch small-scale features of the sea surface wind field (especially at the high-resolution sub-image gridding scale of 3.125 km × 3.125 km), which are not present in the reference ground truth. Within such a context, it must be taken into account that both the reference ASCAT scatterometer and ECMWF model wind speeds are available at the given resolution gridding scale of 12.5 km × 12.5 km and 20 km × 20 km, respectively. Therefore, this could explain some of the differences observed between the reference ground truth wind speed and the X-band SAR-based Azimuth cut-off wind speed retrievals. The output of the X-band COSMO-SkyMed[®] SAR wind direction retrieval approach based on the WT-MRA is shown in Fig. 3a, b, together with the timely and spatially co-located ECMWF and ASCAT scatterometer-based wind direction, respectively. It must be pointed out that the SAR-based wind direction retrieval has been only provided by using a SAR sub-image gridding scale of 12.5 km × 12.5 km, due to the low processing quality of X-band Level 1B DGM ScanSAR Huge Region COSMO-SkyMed[®] SAR measurements. The comparison between the X-band SAR-based WT-MRA wind direction estimation and the reference ground truth (both the scatterometer- and the model-based wind direction) shows a fair agreement with RMSE values equal to 6° and 12° for both the SAR-ASCAT and the SAR-ECMWF wind direction comparisons, respectively. Experimental results agree with previous ones, demonstrating that some of the differences observed between the reference ground truth and the X-band SAR-based WT-MRA wind direction retrievals can be explained by considering the different spatial gridding resolution scale of both modeled (ECMWF) and remotely sensed (SAR and ASCAT) wind direction estimation products.

Other results are summarized in the scatter plots of Fig. 4, where the 12.5 km × 12.5 km SAR-based wind speed and wind direction retrievals are consistently compared with respect to the 12.5 km × 12.5 km ASCAT scatterometer reference wind speed and wind direction, respectively, for the whole processed COSMO-SkyMed[®] SAR data

**COSMO-SkyMed[®] for
coastal marine
applications**

G. Benassai et al.

Title Page

Abstract

Introduction

Conclusions

References

Tables

Figures



Back

Close

Full Screen / Esc

Printer-friendly Version

Interactive Discussion



set. The comparison between the X-band COSMO-SkyMed[®] SAR-based wind field retrievals and ECMWF model wind data will be presented in the next section in terms of sea wave numerical simulations. Experimental results agree with the previous thus demonstrating the consistency of X-band COSMO-SkyMed[®] SAR-derived wind field estimations with respect to the ASCAT scatterometer reference ground truth. In detail, the COSMO-SkyMed[®] SAR-ASCAT wind speed inter-comparison (see Fig. 4a) provides a mean error (μ) value of -0.73 ms^{-1} , a standard deviation (σ) value of 2.07 ms^{-1} and an RMSE value of 2.19 ms^{-1} . On the other side, the COSMO-SkyMed[®] SAR-ASCAT wind direction inter-comparison (see Fig. 4b) provides a mean error (μ) value of 1.71° , a standard deviation (σ) value of 18.88° and an RMSE value of 18.95° . These results effectively demonstrate the consistency of X-band COSMO-SkyMed[®] SAR-derived wind field retrievals with respect to the ASCAT scatterometer ground truth. This latter both suffers from uncertainty over the maritime coastal areas and it is not able to capture small-scale features, which can in turn be revealed by means of SAR data. Such results demonstrate the effectiveness of both the X-band Azimuth cut-off model function and the WT-MRA technique presented in Sect. 2.1 to get consistent wind speed and wind direction estimation, respectively, even through X-band SAR data. Furthermore, experimental results show the full benefits of X-band Level 1B DGM ScanSAR Huge Region mode COSMO-SkyMed[®] SAR data as alternative source of wind field estimation.

4.2 Sea wave numerical simulations

In this sub-section, sea wave numerical simulations of SWAN model are described with respect to some relevant wave storms recorded in the considered test area during the winter season of 2010 (see Table 2). Sea wave numerical simulations have been accomplished by using different wind field products:

- National and Regional Buoys wave field data;

COSMO-SkyMed[®] for coastal marine applications

G. Benassai et al.

Title Page

Abstract

Introduction

Conclusions

References

Tables

Figures



Back

Close

Full Screen / Esc

Printer-friendly Version

Interactive Discussion



- Blended wind field products provided by buoys wave field data and ECMWF model winds;
- Blended wind field products provided by buoys wave field data and X-band COSMO-SkyMed[®] SAR-derived wind field estimations;
- Blended wind field products provided by X-band COSMO-SkyMed[®] SAR-derived wind field estimations and ECMWF winds.

A first meaningful set of results relevant to the application of SWAN model is shown in Fig. 5 with respect to the wave storm of 8–10 November 2010 (see Table 2). In this case, neither the maximum wave heights nor the time evolution of the storm are properly simulated with the wind field forcing provided by ECMWF model winds. In fact, the maximum values of H_s , which are obtained by using both ECMWF model winds and buoys wave field data only, are 5.5 m and 4.0 m, respectively, which are both shifted 15 h earlier. However, these higher maximum wave heights may be overestimated because on the poor amount of data inside the spatial domain of the considered wave storm. The use of a blended wind field product provided by COSMO-SkyMed[®] SAR-derived wind field estimations and ECMWF model winds gives more accurate results, with an underestimation of 0.5 m in H_s (3.5 m instead of 4.0 m), a more accurate resemblance of the storm and a lower temporal shift, as confirmed by the visual inspection of Fig. 5.

A second meaningful set of results relevant to the application of SWAN model is shown in Fig. 6 with respect to the wave storm of 17–18 December 2010 (see Table 2). The sea wave numerical simulation accomplished by using the blended COSMO-SkyMed[®]-ECMWF wind field products shows that the COSMO-SkyMed[®] SAR-derived wind field estimations are able to catch the changing storm characteristics, although the peaks of the wave storm are quite underestimated. In fact, the blended wind field product provided by COSMO-SkyMed[®] SAR-derived wind field estimations and ECMWF model winds retrieves the peak value of H_s , which numbers 3.5 m, instead of 5.0 m.

COSMO-SkyMed[®] for coastal marine applications

G. Benassai et al.

Title Page	
Abstract	Introduction
Conclusions	References
Tables	Figures
◀	▶
◀	▶
Back	Close
Full Screen / Esc	
Printer-friendly Version	
Interactive Discussion	



**COSMO-SkyMed[®] for
coastal marine
applications**

G. Benassai et al.

Title Page

Abstract

Introduction

Conclusions

References

Tables

Figures

◀

▶

◀

▶

Back

Close

Full Screen / Esc

Printer-friendly Version

Interactive Discussion



This result is less accurate than the one obtained by using a wind field forcing provided by ECMWF model winds only, mainly because of the lower time resolution of the wind data and in spite of the higher spatial resolution. In fact, the wave storm event presents a quite fast time evolution, which cannot be interpreted by using wind field data with a temporal interval of 12–24 h. Compared to both buoys wave field observations and ECMWF model winds, very effective results are obtained with the blended wind field products provided by COSMO-SkyMed[®] SAR-derived wind field estimations and ECMWF model winds. More generally, numerical simulations demonstrate that the SWAN model allows providing significant and accurate sea wave estimations even by using blended wind field product composed by both model and remotely sensed wind field data. In detail, the blended use of COSMO-SkyMed[®] SAR wind field estimations and ECMWF model data represents a consistent wind forcing for both the SWAN model and the sub-sequent retrieval of wind-wave interaction parameters.

A third meaningful set of results relevant to the application of the SWAN model is shown in Fig. 7 with respect to the wave storm of 23–25 December 2010 (see Table 2). Numerical simulations agree with previous experimental results. In particular, the blended wind field product provided by COSMO-SkyMed[®] SAR-derived wind field estimations and ECMWF model winds allows improving the retrieval of the SWAN-based wind-wave interaction parameters especially in the first part of the wave storm, where numerical simulations accomplished with ECMWF model winds tends to provide an H_s value overestimation. Moreover, the storm severity underestimation provided by using a blended wind field product composed by both model and remotely sensed wind field data is confined in a mean difference of about 1.0 m (20 % of its maximum value).

The main differences experienced among the three considered wave storms, in terms of numerical simulations, can be summarized as follows:

- Numerical simulations carried out with ECMWF model winds properly describe the sea storms at the peak with regard to the significant wave heights H_s . The only exception is represented by the first wave storm (see Fig. 5 and Table 2), where the peak value of H_s is overestimated of about 38 %. With regard to the

[Title Page](#)
[Abstract](#)
[Introduction](#)
[Conclusions](#)
[References](#)
[Tables](#)
[Figures](#)
[⏪](#)
[⏩](#)
[◀](#)
[▶](#)
[Back](#)
[Close](#)
[Full Screen / Esc](#)
[Printer-friendly Version](#)
[Interactive Discussion](#)


wave storm duration, the first two storms are properly described (see Figs. 5 and 6, respectively, and Table 2), while the third one exhibits an overestimation of 9 % (see Fig. 7 and Table 2).

b) Numerical simulations carried out with a blended wind field product provided by ECMWF model winds and COSMO-SkyMed[®] SAR-derived wind field estimations better follow the significant wave heights at the peak for the first wave storm (see Fig. 5 and Table 2), while for the other two wave storms there is an underestimation of the peak significant wave height of 32 % and 15 %, respectively (see Figs. 6 and 7, respectively, and Table 2). Taking into account the wave storm duration, the results agree with the buoys wave field data for both the first and third wave storms (see Figs. 5 and 7, respectively, and Table 2) and give an underestimation of 37 % for second wave storm (see Fig. 6 and Table 2).

4.3 Coastal vulnerability assessment

In this sub-section, some meaningful experimental results are presented and discussed, which are relevant to the coastal management application of the SWAN model for coastal vulnerability assessment purposes. In detail, the coastal vulnerability assessment is here provided for the test area of Sele coastal plain with respect to the storm impact. The assessment is performed by using the different wind field forcings described in the Sect. 4.2, in terms of both short-term and long-term erosion indexes, the coastal wave climate features and the morpho-sedimentary characteristic of the beach, measured on a number of profiles along the coastal area described in (Di Paola, 2011; Alberigo et al., 2012). The width beach classification is reported in Table 3, while both the details and the beach profile characteristics of coastal Sele plain are shown in Figs. 8 and 9, respectively (Di Paola, 2011; Alberigo et al., 2012).

The low coastline under study presents different morphological and anthropic features, which allow distinguishing some different stretches of coastline: (1) the first one, extending from the mouth of river Picentino till the river Asa (Fig. 8a), shows small

beaches and strong urbanization; (2) the second one, extending from the mouth of the river Tusciano to the mouth of the river Sele, is in part still intact with natural beach features enough preserved (with the exception of the Sele mouth, where there is a strong urbanization); (3) the third one reaches the old town of Paestum and the city of Agropoli towards the South, and is characterized by wider beaches with almost preserved dunes.

The beaches of the first section are mainly sandy, sometimes gravelly. In the past the main sources of sediments were the rivers Irno and Picentino, which were also supplied by a dense set of watersheds between the carbonate slopes of the months of Pastena. Numerous hydraulic dams have greatly reduced the sediment supply to the mouths of the two rivers; moreover, there is also an uninterrupted series of structures, which occupy the narrow coastal strip blocking the natural and vital link between the inland and the coastline. The strong anthropic impact along the beaches is also confirmed by a number of sewage outlets protected by concrete structures and some shore protection works (small detached longitudinal breakwaters, adherent breakwaters) placed here and there to protect single infrastructures and sometimes the coastal road (Fig. 8a, b).

The second coastal section, marked by the river mouths of Tusciano and Sele, shows a wider beach and a lower anthropogenic load, with some exceptions. In fact, proceeding from the Tusciano mouth southwards, the amplitude of the beach gradually increases with finer sand sediments, allowing the establishment of numerous beach resorts. On the left bank of river Sele, a more intense anthropogenic load is experienced, with the presence of a holiday beach resort which corresponds to a narrower beach and a higher intensity of wave attack, evidenced by several pines located directly on the beach, due to a retreat of several tens of meters (Fig. 8e, f).

The southward limit of the physiographic unit, marked by the rivers Capodifiume and Solofrone, shows wider beaches with fine sand and a lower anthropic load, with also a protected area for the preservation of the natural dune habitat (Fig. 8g, h).

COSMO-SkyMed® for coastal marine applications

G. Benassai et al.

Title Page

Abstract Introduction

Conclusions References

Tables Figures

⏪ ⏩

◀ ▶

Back Close

Full Screen / Esc

Printer-friendly Version

Interactive Discussion



Following the detailed description of the test area and the relevant morpho-sedimentary analysis (Di Paola, 2011; Alberigo et al., 2012), some meaningful results are presented and discussed with respect to the application of the SWAN model for coastal vulnerability assessment purposes.

In Fig. 10, it is shown the calculation of the run-up distance as a function of the individual coastal beach profiles defined above, whose lowest values are provided for the profiles that have high beach width (i.e. beach profiles P8–P10 shown in Fig. 9). This result can be simply explained since, in the dimensional wave run-up calculations, the only beach feature entering in the Stockdon formula is the beach slope, consequently the run-up distance is maximum for the beach profiles of the last stretch of coastline. On the other hand, in the non-dimensional calculations, the lower values of the distance are inversely proportional to the emerged beach width (which makes the run-up distance non-dimensional). This circumstance diminishes the vulnerability for the last profiles, which exhibit higher beach width values. The trend shown in Fig. 10 is further observed for each storm considered in this study, with some differences that highlight the key-role played by the significant wave heights. In fact, the run-up distance evaluated for the second wave storm (see Table 2) is greater than the one associated with the other two considered storms (see Table 2), which both exhibit a lower value of H_s .

The calculation of the potential beach retreat as a function of the individual profiles is shown in Fig. 11. This quantity is proportional to the significant wave height, which increases the sea water level as well as the breaking water depth, and is inversely proportional to the particle size. As a matter of fact, the retreat is considerably lower for the beach profiles P1 and P5 shown in Fig. 9, whose particle size presents an order of magnitude higher than the other ones. The trend shown in Fig. 11 is observed for each wave storm considered in this study, with some differences that highlight the key-role played by both significant wave heights and the sea water level. In fact, the retreat associated with the second wave storm is greater than the ones occurred in the other two considered wave storms, as shown in Fig. 10.

**COSMO-SkyMed® for
coastal marine
applications**

G. Benassai et al.

Title Page

Abstract

Introduction

Conclusions

References

Tables

Figures

◀

▶

◀

▶

Back

Close

Full Screen / Esc

Printer-friendly Version

Interactive Discussion



With respect to the coastal vulnerability evaluation, which is performed with sea-wave numerical simulations by using the different wind field forcings described in Sect. 4.2, some meaningful results are shown in Figs. 12 and 13, which are relevant to the evaluation of both the run-up distance and the beach retreat, respectively, for the first wave storm described in Table 2. It can be noted that the numerical simulation results, gathered by using the blended COSMO-SkyMed[®]-ECMWF wind field forcing, show a good agreement with respect to the information provided by buoys wave field data. Conversely, numerical simulation results gathered by only using the ECMWF wind field forcing show an overestimation of about 30 % with respect to the information provided by buoys wave field data. Notwithstanding this, a very effective agreement is experienced between the numerical simulation results gathered by only using either ECMWF model data or buoys wave field data for both the second and the third wave storms depicted in Table 2. As a matter of fact, a consistent agreement is also provided for the evaluation of both the run-up distance and the beach retreat relevant to these other two wave storms.

The comparison of the experimental results, which are relevant to the coastal vulnerability index evaluated through the significant wave parameters provided at the output of sea-wave numerical simulations run with different wind field forcing data, is shown in Fig. 14, for the first wave storm (see Table 2). Experimental results demonstrate that the vulnerability index, which is evaluated with respect to the sea-wave numerical simulations accomplished by means of a blended COSMO-SkyMed[®]-ECMWF wind field data, show a very good agreement with the ones obtained with buoys wave field data. In the other two wave storms (i.e. the second and the third ones), the underestimation of the vulnerability index, which is experienced by considering the blended COSMO-SkyMed[®]-ECMWF wind field forcing at the input of sea-wave numerical simulations, is much lower than the one associated with the run-up distance and beach retreat. This result takes into account that the value of the vulnerability index corresponds to a range of values of the above-mentioned parameters, which therefore reduces the index differences.

**COSMO-SkyMed[®] for
coastal marine
applications**

G. Benassai et al.

Title Page

Abstract

Introduction

Conclusions

References

Tables

Figures



Back

Close

Full Screen / Esc

Printer-friendly Version

Interactive Discussion



In order to perform a final assessment of the coastal vulnerability that could be independent on the individual wave storm, an average vulnerability index is evaluated over the three-reference wave storms occurred in the winter season of 2010 (see Fig. 15). The proposed index is referred to the mean values of the indicators X_{\max}/l and R_{\max}/l , which are properly evaluated for each considered wave storm. The comparison of the experimental results, which are experienced for the numerical simulations run with either a blended COSMO-SkyMed[®]-ECMWF wind field forcing or the buoys wave field data, respectively, shows that the differences in the coastal vulnerability index are further reduced to a maximum of one unit (with the exception of profile P9 in Fig. 9), thus reinforcing the above statement and confirming the previous results.

5 Conclusions

In this paper, X-band COSMO-SkyMed[®] SAR data are first successfully experimented as wind field forcing of coastal wind-wave oceanographic modeling for both sea-wave numerical simulation and coastal vulnerability assessment purposes. The SAR data set consists of 60 X-band VV-polarized Level 1B DGM ScanSAR Huge Region COSMO-SkyMed[®] SAR measurements, collected in the test area during the winter season of 2010. The wind-wave oceanographic modeling is based on the third-generation SWAN model, while the coastal vulnerability assessment is accomplished by means of a key parameter known as impact index.

Experimental results firstly show how X-band COSMO-SkyMed[®] SAR-derived wind field estimations can be effectively used to force both the SWAN and the coastal vulnerability assessment models for oceanographic applications. Meaningful tests are successfully accomplished in the Southern Tyrrhenian Sea basin, where some significant wave storms have been both recorded and analyzed. This is of both scientific and the operational relevance.

In detail, with respect to the sea-wave numerical simulations, very consistent and accurate results are obtained by forcing the SWAN model with COSMO-SkyMed[®]

Title Page

Abstract

Introduction

Conclusions

References

Tables

Figures



Back

Close

Full Screen / Esc

Printer-friendly Version

Interactive Discussion



SAR-derived wind field estimations. These latter are able to catch the trend of the wave storms, further providing consistent estimations of H_s with a slightly underestimation of 20–30 % at the storm peak. This important result can be used for further research activities relevant to the use of COSMO-SkyMed[®] SAR data as alternative integrated source of sea surface wind field information. Furthermore, experimental results effectively demonstrate that a blended wind product including both ECMWF model data and COSMO-SkyMed[®] SAR-derived wind field estimations can provide valuable improvements of wind-wave interaction modeling.

With respect to the coastal vulnerability assessment, the analysis is successfully accomplished by covering the following aspects:

1. Comparison between the responses of different beach profiles with respect to the actions of significant wave storms with the purpose to highlight the role of geomorphological parameters (sediment size, intertidal beach slope and width of the emerged beach) for each profile.
2. Comparison among the experimental results of the several sea wave numerical simulations accomplished by using both blended COSMO-SkyMed[®]-ECMWF wind fields and ECMWF model data only (both validated with respect to buoys wave field data), in terms of both the wave storm reconstruction and the calculations of parameters affecting the coastal vulnerability.
3. Calculation of a coastal vulnerability index obtained with the mean values of the parameters calculated for each wave storm, in order to evaluate the suitability of the blended COSMO-SkyMed[®]-ECMWF wind field data for coastal management purposes.

With respect to the storm reconstruction, experimental results demonstrate that the sea wave numerical simulations accomplished with blended COSMO-SkyMed[®]-ECMWF wind field forcing closely follow the true significant wave height of the first wave storm (see Table 2). In fact, a slight H_s underestimation of 9 % is provided against the H_s

COSMO-SkyMed[®] for coastal marine applications

G. Benassai et al.

Title Page

Abstract

Introduction

Conclusions

References

Tables

Figures



Back

Close

Full Screen / Esc

Printer-friendly Version

Interactive Discussion



overestimation of 38 % provided by considering sea wave numerical simulations accomplished with ECMWF model wind forcing only. However, for the other two wave storms (i.e. the second and the third ones in Table 2), experimental results provide an H_s underestimation of 32 % and 15 %, respectively.

5 With respect to the calculation of the run-up distance, experimental results relevant to the sea wave numerical simulations accomplished by using the blended COSMO-SkyMed[®]-ECMWF wind field forcing show a good agreement with respect to the results obtained by using buoys wave field data, especially for the first wave storm considered in the paper (see Table 2). In fact, an underestimation of the parameters of about 30 % and 15 % is provided with respect to the second and the third wave storm, respectively.
10 With regard to the calculation of the beach retreat, sea wave numerical simulation results obtained by using the blended COSMO-SkyMed[®]-ECMWF wind field forcing show a very good agreement with the results experienced by using the buoys wave field data for the first wave storm of Table 1. On the other side, both a significant (50 %) and slight (10 %) underestimation of the parameters is provided for the second and the third wave storms in Table 2, respectively.
15

The retrieval differences, which are provided through the previous analysis, decrease when the calculation of the vulnerability index is carried out, since the range of the last parameter corresponds to an interval of values of the parameters affecting the coastal vulnerability. Within such a framework, experimental results relevant to the first wave storm show a very good agreement between the sea wave numerical simulations accomplished by using both blended COSMO-SkyMed[®]-ECMWF wind field forcing and buoys wave field data. On the other side, an underestimation of 15 % is provided for the coastal vulnerability index calculations with respect to both the second and the third wave storms in Table 2. This underestimation is even lower when a global vulnerability index is calculated, based on the mean values of the parameters affecting the coastal vulnerability taken for each storm.
20
25

In conclusion, the results obtained with the use of blended COSMO-SkyMed[®]-ECMWF data are satisfactory in terms of coastal vulnerability classification of the

COSMO-SkyMed[®] for coastal marine applications

G. Benassai et al.

Title Page

Abstract

Introduction

Conclusions

References

Tables

Figures



Back

Close

Full Screen / Esc

Printer-friendly Version

Interactive Discussion



examined shoreline. In fact, the coastal vulnerability index obtained through the blended COSMO-SkyMed[®]-ECMWF wind field data is consistent with the one obtained by using buoys wave field data, with a slight difference that does not affect the classification of coastal criticality.

- 5 *Acknowledgements.* COSMO-SkyMed[®] SAR data used in this study are provided by Italian Space Agency under the scientific research project entitled “Improvement of Oceanic Modelling for Coastal Management by means of COSMO-SkyMed[®] SAR data” (Project ID 1500). Authors would like to acknowledge Di Paola for beach morphological data and useful discussions.

References

- 10 Alberico, I., Amato, V., Aucelli, P. P. C., Di Paola, G., Pappone, G. and Roskopf, C. M.: Historical and recent changes of the Sele River coastal plain (Southern Italy): natural variations and human pressures, *Rend. Lincei*, 23, 3–12, doi:10.1007/s12210-011-0156-y, 2012.
- Benassai, G.: Introduction to Coastal Dynamics and Shoreline Protection, Wit Press, Southampton, 1, 1–356, 2006.
- 15 Benassai, G. and Ascione, I.: Implementation and validation of wave watch III model offshore the coastlines of Southern Italy, in: Proceedings of 25th International Conference on Offshore Mechanics and Arctic Engineering 2006-92555, Hamburg, Germany, 4-9 June 2006, 553-560, 2006.
- Benassai, G., Chirico, F., and Corsini, S.: Una metodologia per la definizione del rischio da inondazione costiera, *Studi Costieri*, 16, 51–72, 2009.
- 20 Booij, N., Ris, R. C., and Holthuijsen, L. H.: A third-generation wave model for coastal regions, Part I: Model description and validation, *J. Geophys. Res.*, 104, 7649–7666, 1999.
- Bruun P.: Sea level rise as a cause of shore erosion, *J. Waterw. Port C-Div.*, 88, 117–130, 1962.
- Carter, T. R., Parry, M. L., Nishioka, S., and Harasawa, H.: Technical guidelines for assessing climate change impacts and adaptation, University College London, London, and Centre for
- 25 Global Environmental Research, Tskuba, Japan, 1994.
- Chapron, B., Fouhaily, T. E., and Kerbaol, V.: Calibration and validation of ERS wave mode products, *Inst. Fr. De Rech. pour l’Exploit de la Mer*, Brest, France, Doc. DRO/OS/95-02, 1995.

COSMO-SkyMed[®] for coastal marine applications

G. Benassai et al.

Title Page

Abstract

Introduction

Conclusions

References

Tables

Figures



Back

Close

Full Screen / Esc

Printer-friendly Version

Interactive Discussion



COSMO-SkyMed® for coastal marine applications

G. Benassai et al.

Title Page

Abstract

Introduction

Conclusions

References

Tables

Figures

◀

▶

◀

▶

Back

Close

Full Screen / Esc

Printer-friendly Version

Interactive Discussion



- Diez, P. G., Perillo, G. M. E., and Picolo, M. C.: Vulnerability to seal-level rise on the coast of the Buenos Aires Province, *J. Coastal Res.*, 23, 119–126, 2007.
- Di Paola, G.: Geological and geo-morphological characterization of coastal Sele Plain (Campania, Italy) and considerations about its vulnerability, Ph.D. Thesis, Università degli Studi del Molise, Italy, 2011.
- 5 Du, Y., Vachon, P. W., and Wolfe, J.: Wind direction estimation from SAR images of the Ocean using wavelet analysis, *Can. J. Remote Sens.*, 28, 498–509, 2002.
- Gornitz, M. V., Daniels, R. C., White, T. W., and Birdwell, K. R.: The development of a coastal risk assessment database: vulnerability to sea-level rise in the U.S. southeast, *J. Coastal Res.*, Special Issue 12, 327–338, 1994.
- 10 Gornitz, V. M., Beaty, T. W., and Daniels, R. C.: A coastal hazards data base for the U.S. West Coast, Carbon Dioxide Information Analysis Center, Oak Ridge National Laboratory, Oak ridge, Tennessee, 162 pp., 1997.
- Harlan Jr., J. A.: Short Time Scale Effects on High Frequency Radar-Derived Current Velocity Measurements, Ph.D. Dissertation, University of Colorado, Bolder, 2005.
- Hasselmann, K., Barnett, T. P., Bouws, E., Carlson, H., Cartwright, D. E., Enke, K., Ewing, J. A., Gienapp, H., Hasselmann, D. E., Kruseman, P., Meerburg, A., Müller, P., Olbers, D. J., Richter, K., Sell, W., and Walden, H.: Measurements of wind-wave growth and swell decay during the Joint North Sea Wave Project (JONSWAP), *Dtsch. Hydrogr. Z. Suppl.*, 12, 1–95, 1973.
- 20 Holthuijsen, L. H., Booij, N., and Ris, R. C.: A spectral wave model for the coastal zone, in: Proceedings of the 2nd International Symposium on Ocean Wave Measurement and Analysis, New Orleans, 630–641, 1993.
- Italian Space Agency (ASI) – COSMO-SkyMed Mission: COSMO-SkyMed System Description and User Guide, available at: <http://www.asi.it/it/flash/osservare/cosmoskymed/>, 2012.
- 25 Janssen, P.: The Interaction of Ocean Waves and Wind, Cambridge University Press, UK, 2004.
- Kerbaol, V., Chapron, B., and Vachon, P. W.: Analysis of ERS-1/2 synthetic aperture radar wave mode images, *J. Geophys. Res.*, 103, 7833–7846, 1998.
- 30 Korsbakken, E., Johannessen, J. A., and Johannessen, O. M.: Coastal wind field retrievals from ERS synthetic aperture radar image, *J. Geophys. Res.*, 103, 7857–7874, 1998.
- Kriebel, D. L. and Dean, R. G.: Convolution method for time-dependent beach-profile response, *J. Waterw. Port C-Div.*, 119, 204–207, 1993.

COSMO-SkyMed® for coastal marine applications

G. Benassai et al.

Title Page

Abstract

Introduction

Conclusions

References

Tables

Figures

◀

▶

◀

▶

Back

Close

Full Screen / Esc

Printer-friendly Version

Interactive Discussion



Lee, P. H. Y., Barter, J. D., Beach, K. L., Hindman, C. L., Lake, B. M., Rungaldier, H., Shelton, J. C., Williams, A. B., Yee, R., and Yuen, H. C.: X band microwave backscattering from ocean waves, *J. Geophys. Res.*, 100, 2591–2611, 1995.

Mallat, S. G.: A theory for multiresolution signal decomposition: the wavelet representation, *IEEE T. Pattern Anal.*, 11, 674–693, 1989.

Migliaccio, M., Montuori, A., and Nunziata, F.: X-band Azimuth cut-off for wind speed retrieval by means of COSMO-SkyMed SAR data, in: Proceedings of IEEE/OES Baltic International Symposium, Klaipeda, Lithuania, 8–10 May 2012, 1–4, 2012.

Montuori, A., Migliaccio, M., and Nunziata, F.: Wind speed estimation in the Tyrrhenian Sea by means of X-band COSMO-SkyMed SAR data, in: Proceedings of Tyrrhenian Workshop on Advances in Radar and Remote Sensing 2012, Naples, Italy, 12–14 September 2012.

Schiavulli, D., Sorrentino, A., and Migliaccio, M.: An automatic procedure for scalloping suppression and homogeneity analysis of sea X-band CSK SAR images, *Atti della Fondazione Giorgio Ronchi – Anno LXVII*, 66, 27–38, 2011.

Schiavulli, D., Sorrentino, A., and Migliaccio, M.: An innovative technique for postprocessing descalloping, *IEEE Geosci. Remote S.*, PP, 1–4, 2012.

Schulz-Stellenfleth, J. and Lehner, S.: Measurement of 2-D sea surface elevation fields using complex synthetic aperture radar data, *IEEE T. Geosci. Remote*, 42, 1149–1160, 2004.

Stockdon, H. F., Holman, R. A., Howd, P. A., and Sallenger, A. H.: Empirical parameterization of setup, swash, and run-up, *Coast. Eng.*, 53, 573–588, 2006.

Tolman, H. L.: A third-generation model for wind waves on slowly varying, unsteady and inhomogeneous depths and currents, *J. Phys. Oceanogr.*, 21, 782–797, 1991.

Tolman, H. L.: User manual and system documentation of WAVEWATCH-III version 1.15, Technical Note 151, NOAA/NWS/NCEP/OMB, Washington DC, United States, 97 pp., 1997.

Tolman, H. L.: User manual and system documentation of WAVEWATCH-III version 1.18, Technical Note 166, NOAA/NWS/NCEP/OMB, Washington DC, United States, 110 pp., 1999.

Tolman, H. L.: User manual and system documentation of WAVEWATCH III version 3.14, Technical Note 276, NOAA/NWS/NCEP/MMAB, Washington DC, United States, 194 pp., 2009.

WAMDI Group: The WAM model – a third generation ocean wave prediction model, *J. Phys. Oceanogr.*, 18, 1775–1810, 1988.

Whitham, G. B.: *Linear and Nonlinear Waves*, John Wiley, New York, 636 pp., 1974.

COSMO-SkyMed[®] for coastal marine applications

G. Benassai et al.

Title Page

Abstract

Introduction

Conclusions

References

Tables

Figures

◀

▶

◀

▶

Back

Close

Full Screen / Esc

Printer-friendly Version

Interactive Discussion



Table 1. Range variables of each index for the evaluation of vulnerability index.

Variables	Stability 1	Low 2	Moderate 3	High 4
I_R (%)	< 15	15–30	30–50	> 50
I_{Ru} (%)	< 40	40–60	60–80	> 80
I_E (m yr ⁻¹)	< 0.5	0.5–1.0	1.0–2.0	> 2.0

COSMO-SkyMed[®] for coastal marine applications

G. Benassai et al.

Table 3. Beach width classification of the different stretches of coastline.

Beach width L (2010)	Mouth of Picentino (m,%)		Mouth of Tusciano (m,%)		Mouth of Sele (m,%)		Mouth of Solofrone (m,%)	
Wide ($L > 50$ m)	–	–	800	32	–	–	1200	60
Medium ($20 < L < 50$ m)	1200	48	1700	68	2050	82	800	40
Restricted ($L < 20$ m)	1300	52	–	–	350	14	–	–
Defense works	–	–	–	–	100	4	–	–

Title Page

Abstract

Introduction

Conclusions

References

Tables

Figures

⏪

⏩

◀

▶

Back

Close

Full Screen / Esc

Printer-friendly Version

Interactive Discussion



COSMO-SkyMed® for coastal marine applications

G. Benassai et al.

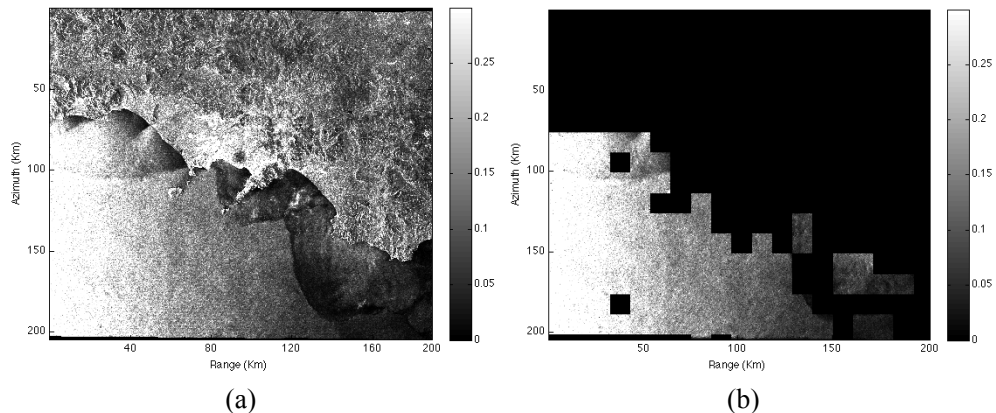


Fig. 1. X-band Level 1B DGM ScanSAR Huge Region COSMO-SkyMed® SAR data acquired on 17 December 2010 at 18:00 UTC. **(a)** VV-polarized NRCS. **(b)** Output of the pre-processing step relevant to the SAR wind field retrieval approach.

[Title Page](#)[Abstract](#)[Introduction](#)[Conclusions](#)[References](#)[Tables](#)[Figures](#)[⏪](#)[⏩](#)[◀](#)[▶](#)[Back](#)[Close](#)[Full Screen / Esc](#)[Printer-friendly Version](#)[Interactive Discussion](#)

COSMO-SkyMed[®] for coastal marine applications

G. Benassai et al.

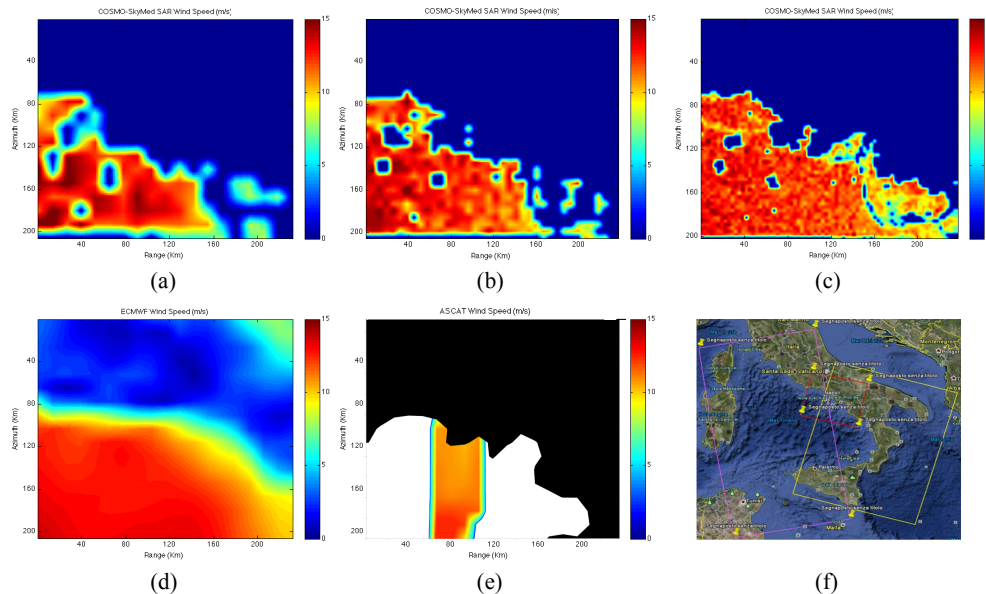


Fig. 2. Experimental results relevant to the SAR-based wind speed estimation for the X-band Level 1B DGM ScanSAR Huge Region COSMO-SkyMed[®] SAR data acquired on 17 December 2010 at 18:00 UTC. **(a–c)** X-band SAR-derived wind speed estimation over a sub-image scale of 12.5 km × 12.5 km, 6.25 km × 6.25 km and 3.125 km × 3.125 km, respectively. **(d)** Reference ground truth provided by timely and spatially co-located ECMWF model wind speed. **(e)** Reference ground truth provided by timely and spatially co-located ASCAT scatterometer wind speed. **(f)** Footprints of the ASCAT scatterometer wind speeds acquired before (purple box) and after (yellow box) with respect to the SAR acquisition, whose footprint is shown red color.

COSMO-SkyMed[®] for coastal marine applications

G. Benassai et al.

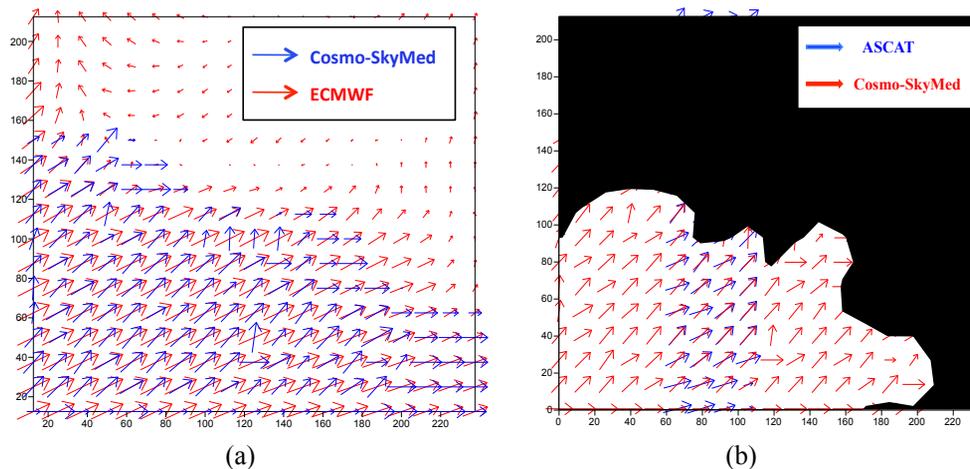


Fig. 3. Experimental results relevant to the SAR-based wind direction estimation for the X-band Level 1B DGM ScanSAR Huge Region COSMO-SkyMed[®] SAR data acquired on 17 December 2010 at 18:00 UTC. **(a)** Comparison between X-band SAR-derived wind direction estimation and the reference ECMWF model wind direction over a sub-image scale of 12.5 km × 12.5 km. **(b)** Comparison between X-band SAR-derived wind direction estimation and the reference ASCAT scatterometer wind direction over a sub-image scale of 12.5 km × 12.5 km.

Title Page

Abstract

Introduction

Conclusions

References

Tables

Figures

◀

▶

◀

▶

Back

Close

Full Screen / Esc

Printer-friendly Version

Interactive Discussion



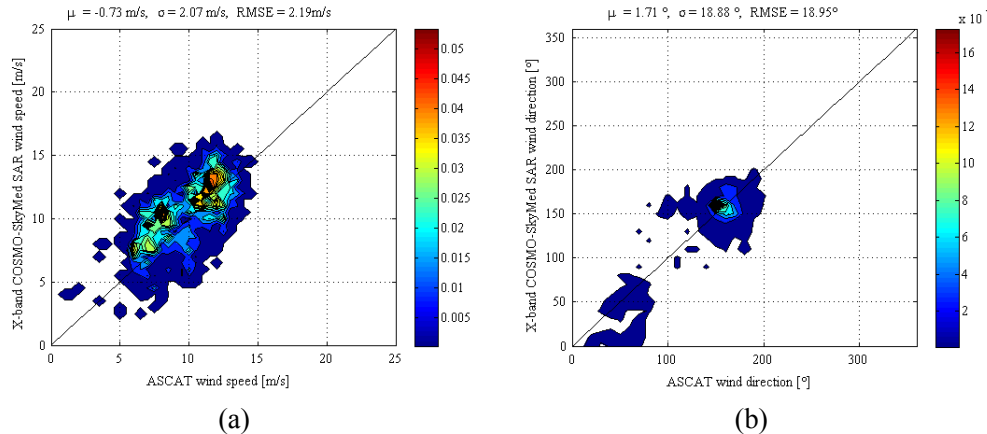


Fig. 4. 2-D probability density scatter plot relevant to the comparison between the 12.5 km × 12.5 km X-band COSMO-SkyMed[®] SAR-derived wind field estimation and the 12.5 km × 12.5 km ASCAT scatterometer reference ground truth, for the whole processed COSMO-SkyMed[®] SAR data set. **(a)** Wind speed inter-comparison scatter plot. **(b)** Wind direction inter-comparison scatter plot.

Title Page

Abstract

Introduction

Conclusions

References

Tables

Figures

◀

▶

◀

▶

Back

Close

Full Screen / Esc

Printer-friendly Version

Interactive Discussion



COSMO-SkyMed[®] for coastal marine applications

G. Benassai et al.

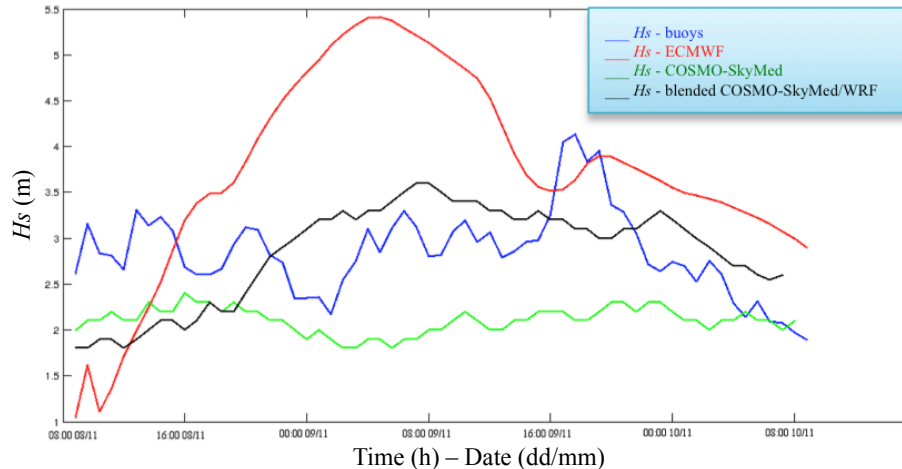


Fig. 5. Simulated and measured significant wave height H_s for the winter storm of 8–10 November 2010. Comparison among buoys (blue line), blended buoys and ECMWF (red line), COSMO-SkyMed[®] SAR (green line), and blended buoys and COSMO-SkyMed[®] SAR-derived wind fields (black line).

Title Page

Abstract

Introduction

Conclusions

References

Tables

Figures

⏪

⏩

◀

▶

Back

Close

Full Screen / Esc

Printer-friendly Version

Interactive Discussion



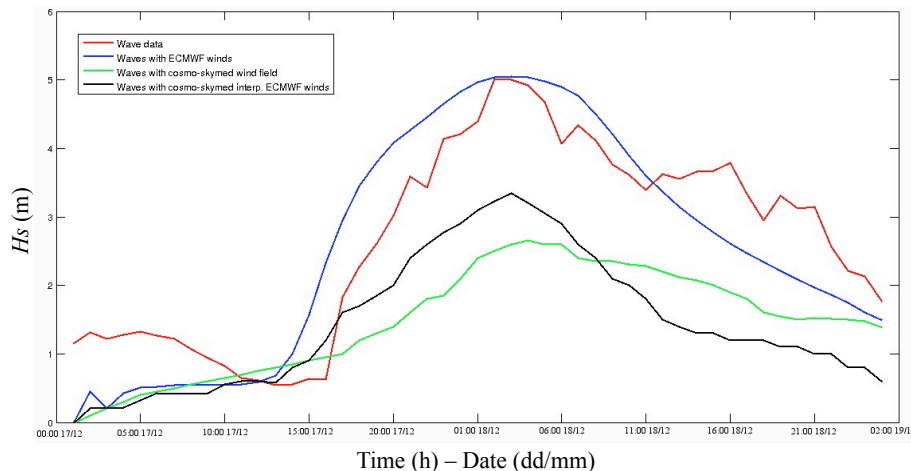


Fig. 6. Simulated and measured significant wave height H_s for the winter storm of 17–18 December 2010. Comparison among buoys (red line), blended buoys and ECMWF (blue line), blended COSMO-SkyMed[®] SAR and ECMWF (black line), and blended buoys and COSMO-SkyMed[®] SAR-derived wind fields (green line).

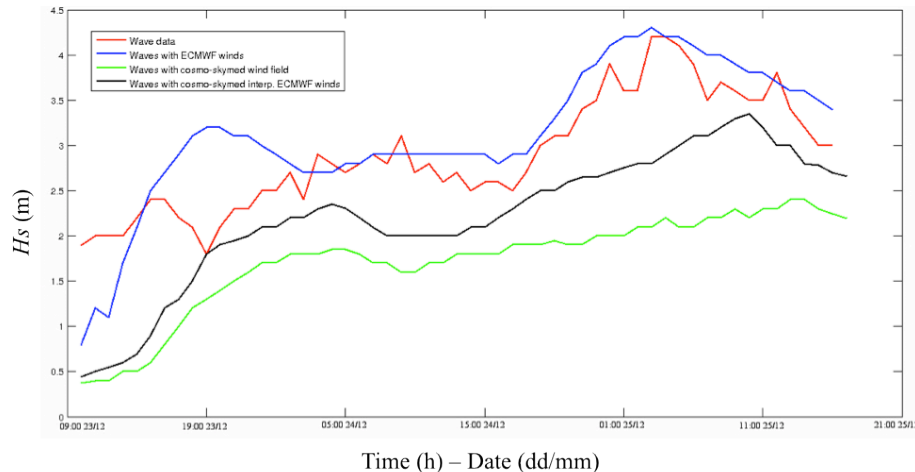


Fig. 7. Simulated and measured significant wave height H_s for the winter storm of 23–25 December 2010. Comparison among buoys (red line), blended buoys and ECMWF (blue line), blended COSMO-SkyMed® SAR and ECMWF (black line), and blended buoys and COSMO-SkyMed® SAR-derived wind fields (green line).

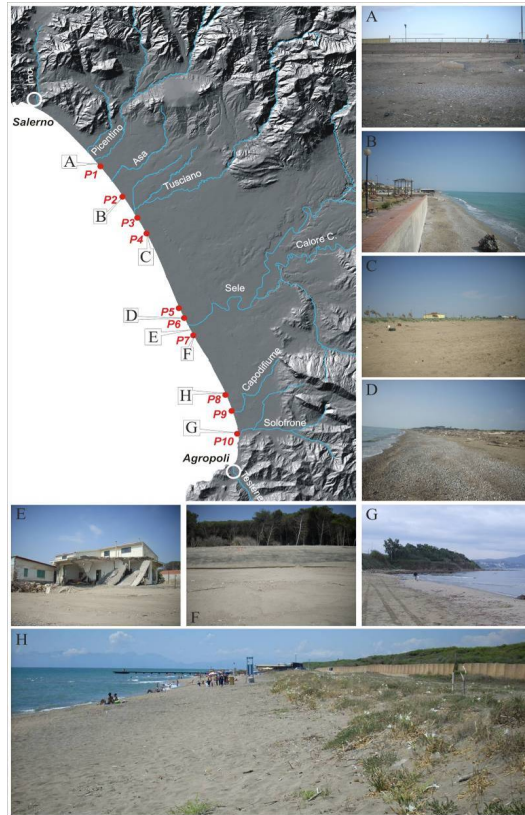


Fig. 8. Detail of the coast Sele Plain: **(A)** profile P1 without dune; **(B)** the littoral zone, near the P2 profile; **(C)** dune on profile P4 with the presence of pioneer vegetation; **(D)** emerged and tidal beach on P6 profile; **(E)** house belonging to the village Merola, located at the left bank of the Sele mouth; **(F)** Profile P7, with carved dune; **(G)** the end of physiographic unit near profile P10; **(H)** dune and emerged beach of profile P8 with the presence of pioneer vegetation on the dune. All the beach profiles are detailed in Fig. 9.

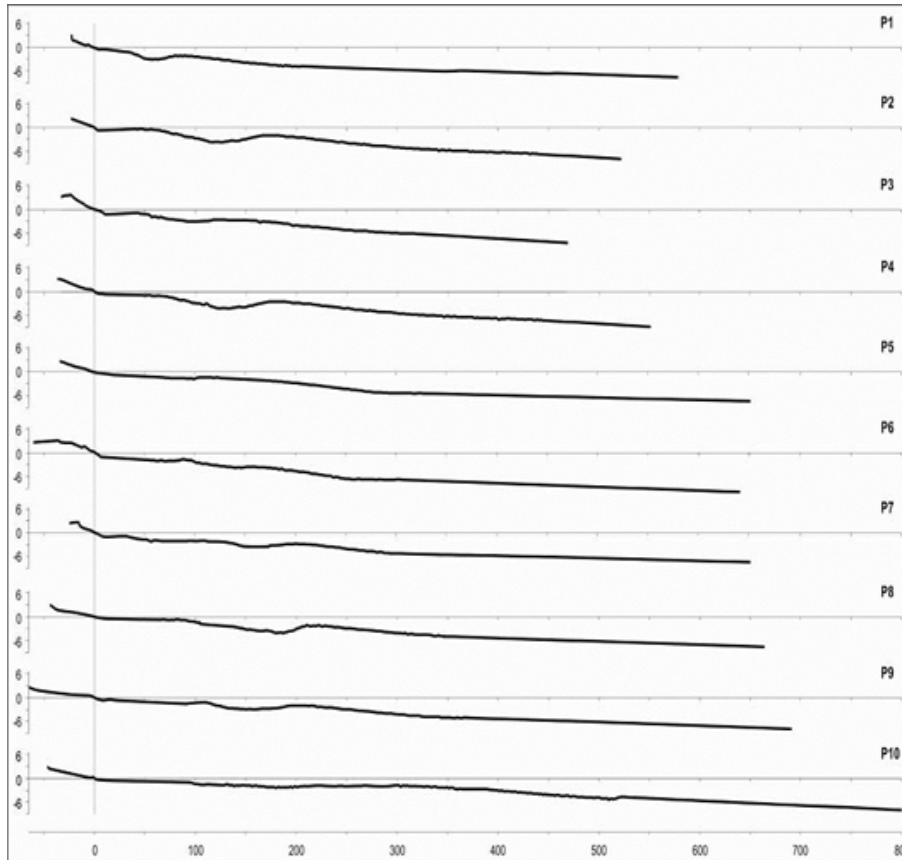


Fig. 9. Topographical beach profiles carried out in the coastal Sele Plain.

Title Page	
Abstract	Introduction
Conclusions	References
Tables	Figures
⏪	⏩
◀	▶
Back	Close
Full Screen / Esc	
Printer-friendly Version	
Interactive Discussion	



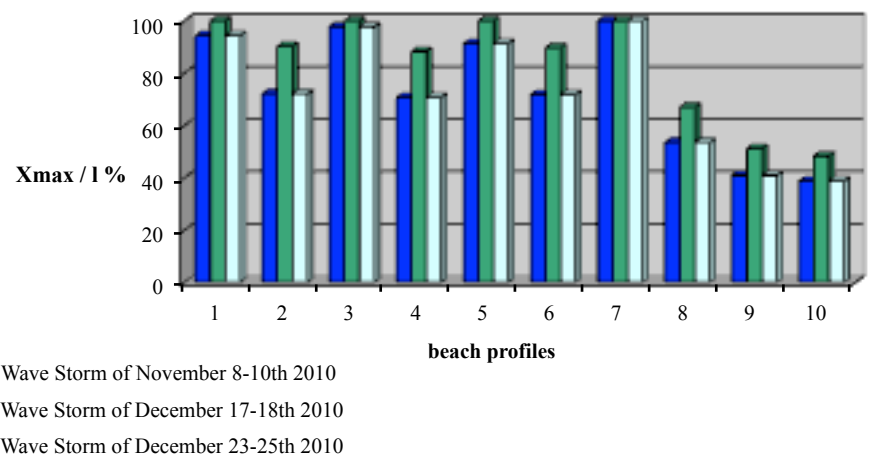


Fig. 10. Non-dimensional run-up distance for the three wave storms of the winter season 2010.

Title Page

Abstract

Introduction

Conclusions

References

Tables

Figures

⏪

⏩

◀

▶

Back

Close

Full Screen / Esc

Printer-friendly Version

Interactive Discussion



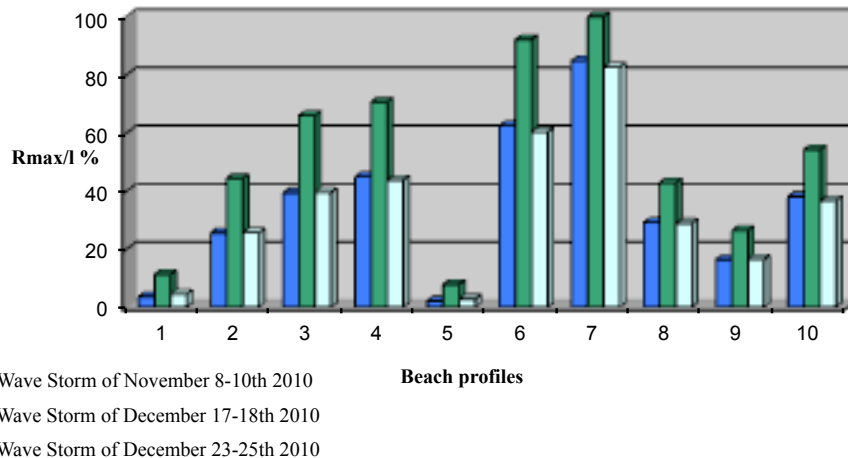


Fig. 11. Non-dimensional beach retreat for the three wave storms of the winter season 2010.

[Title Page](#)

[Abstract](#) [Introduction](#)

[Conclusions](#) [References](#)

[Tables](#) [Figures](#)

[⏪](#) [⏩](#)

[◀](#) [▶](#)

[Back](#) [Close](#)

[Full Screen / Esc](#)

[Printer-friendly Version](#)

[Interactive Discussion](#)



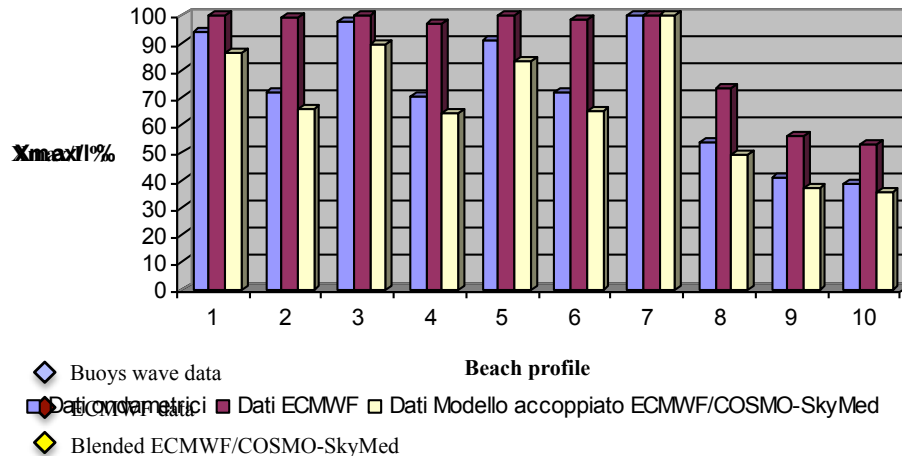


Fig. 12. Comparison of experimental results, which are relevant to the non-dimensional run up distance evaluated for the wave storm of 8–10 November 2010 by using different wind field forcings (i.e. Buoys wave data, ECMWF model data and blended ECMWF-COSMO-SkyMed® wind fields).

[Title Page](#)
[Abstract](#)
[Introduction](#)
[Conclusions](#)
[References](#)
[Tables](#)
[Figures](#)
[⏪](#)
[⏩](#)
[◀](#)
[▶](#)
[Back](#)
[Close](#)
[Full Screen / Esc](#)
[Printer-friendly Version](#)
[Interactive Discussion](#)

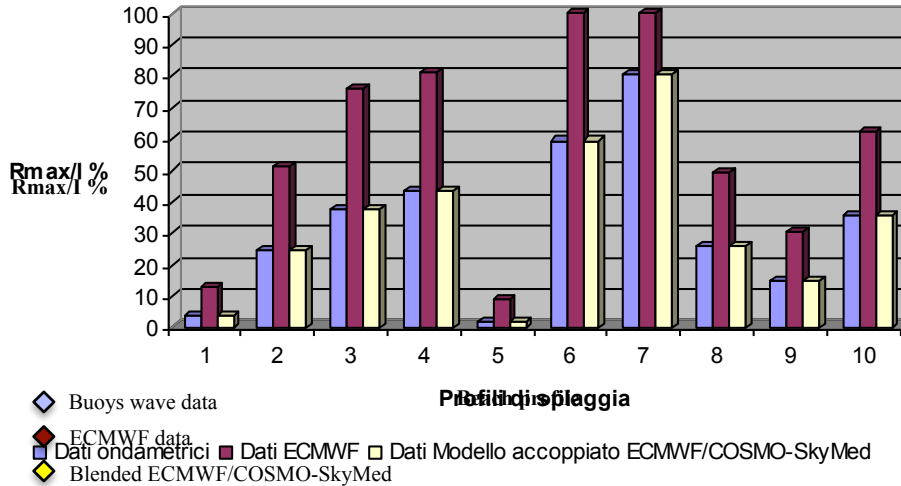



Fig. 13. Comparison of experimental results, which are relevant to the non-dimensional beach retreat evaluated for the wave storm of 8–10 November 2010 by using different wind field forcings (i.e. Buoys wave data, ECMWF model data and blended ECMWF-COSMO-SkyMed® wind fields).

Title Page

Abstract	Introduction
Conclusions	References
Tables	Figures

⏪ ⏩
◀ ▶
Back Close

Full Screen / Esc

Printer-friendly Version

Interactive Discussion



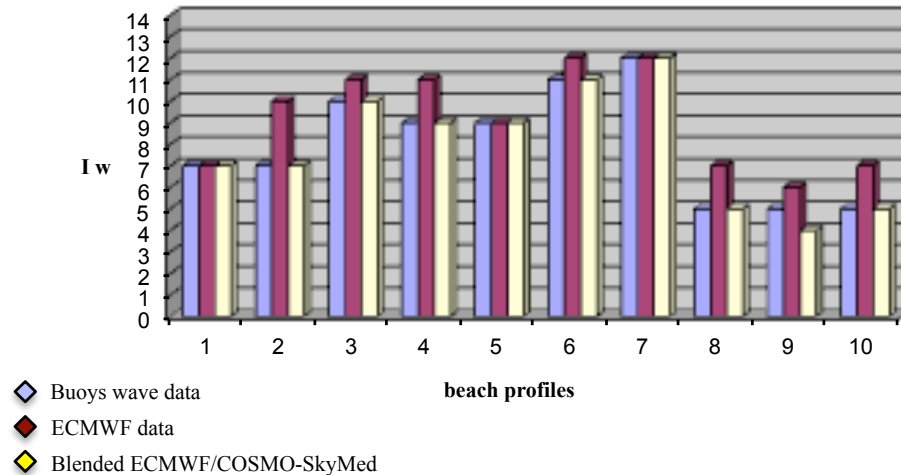


Fig. 14. Coastal vulnerability index evaluated for the wave storm of 8–10 November 2010 by using different wind field forcings (i.e. Buoys wave data, ECMWF model data and blended ECMWF-COSMO-SkyMed® wind fields).

[Title Page](#)
[Abstract](#)
[Introduction](#)
[Conclusions](#)
[References](#)
[Tables](#)
[Figures](#)
[⏪](#)
[⏩](#)
[◀](#)
[▶](#)
[Back](#)
[Close](#)
[Full Screen / Esc](#)
[Printer-friendly Version](#)
[Interactive Discussion](#)

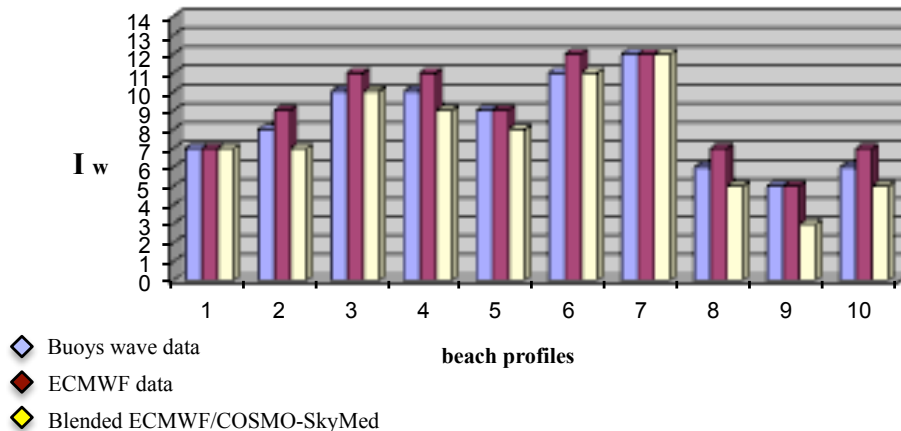


Fig. 15. Average coastal vulnerability index evaluated for the three wave storm of the winter season 2010 by using different wind field forcings (i.e. Buoys wave data, ECMWF model data and blended ECMWF-COSMO-SkyMed® wind fields).

[Title Page](#)

[Abstract](#) [Introduction](#)

[Conclusions](#) [References](#)

[Tables](#) [Figures](#)

[◀](#) [▶](#)

[◀](#) [▶](#)

[Back](#) [Close](#)

[Full Screen / Esc](#)

[Printer-friendly Version](#)

[Interactive Discussion](#)

